LAWRENCE
LIVERMORE
NATIONAL
LABORATORY

LLNL-JRNL-648132

Observations of strong ion-ion correlations in dense plasmas

T. MA, D. A. CHAPMAN, T. DOEPPNER, R. W. Falcone, L. Fletcher, C. Fortmann, E. Galtier, S. H. Glenzer, D. O. Gericke, G. Gregori, J. Hastings, S. LePape, H. J. Lee, B. Nagler, P. NEUMAYER, A. E. Pak, D. Turnbull, J. Vorberger, T. G. White, K. Wunsch, U. Zastrau

December 23, 2013

Physics of Plasmas

Disclaimer

Observations of strong ion-ion correlations in dense plasmas

T. Ma,[1, a)] D. A. Chapman,[2, 3] T. Döppner,[1] R. W. Falcone,[4] L. Fletcher,[5] C. Fortmann,[1, 6] E. Galtier,[5] D. O. Gericke,[3] G. Gregori,[7] J. Hastings,[5] O. L. Landen,[1] S. Le Pape,[1] H. J. Lee,[5] B. Nagler,[5] P. Neumayer,[8] A. Pak,[1] D. Turnbull,[1] J. Vorberger,[9] T. G. White,[7] K. Wünsch,[10] U. Zastrau,[5, 11] and S. H. Glenzer[5]

[1)] *Lawrence Livermore National Laboratory, Livermore, California 94550, USA*

[2)] *Plasma Physics Group, AWE plc, Reading RG7 4PR, United Kingdom*

[3)] *Centre for Fusion, Space and Astrophysics, Department of Physics, University of Warwick, Coventry CV4 7AL, United Kingdom*

[4)] *Physics Department, University of California, Berkeley, CA 94720, USA*

[5)] *SLAC National Accelerator Laboratory, Menlo Park, CA 94025, USA*

[6)] *Department of Physics and Astronomy, University of California, Los Angeles, CA 90095, USA*

[7)] *University of Oxford, Clarendon Laboratory, Oxford OX1 3PU, United Kingdom*

[8)] *Extreme Matter Institute, GSI Helmholtzzentrum für Schwerionenforschung, Planckstr. 1, 64291 Darmstadt, Germany*

[9)] *Max Planck Institut für Physik komplexer Systeme, Nötthnizer Straße 38, 01187 Dresden, Germany*

[10)] *Tessella, 26 The Quadrant, Abington OX14 3YS, United Kingdom*

[11)] *Institute for Optics and Quantum Electronics, Friedrich-Schiller-University, 07743 Jena, Germany*

(Dated: 11 December 2013)

Using simultaneous spectrally, angularly, and temporally resolved x-ray scattering, we measure the pronounced ion-ion correlation peak in a strongly coupled plasma. Laser-driven shock-compressed aluminum at ∼3× solid density is probed with high-energy photons at 17.9 keV created by molybdenum He-α emission in a laser-driven plasma source. The measured elastic scattering feature shows a well-pronounced correlation peak at a wave vector of $k = 4\,\text{Å}^{-1}$. The magnitude of this correlation peak cannot be described by standard plasma theories employing a linear screened Coulomb potential. Advanced models, including a strong short-range repulsion due to the inner structure of the aluminum ions are however in good agreement with the scattering data. These studies have demonstrated a new highly accurate diagnostic technique to directly measure the state of compression and the ion-ion correlations. We have since applied this new method in single-shot wave-number resolved $S(k)$ measurements to characterize the physical properties of dense plasmas.

PACS numbers: 52.27.Gr, 52.25.Os, 71.45.Gm

I. INTRODUCTION

The warm dense matter (WDM) regime of high energy density physics[1] is of particular interest as it encompasses a broad regime of extreme conditions, existing between hot plasmas and condensed matter. It is within the WDM regime that planetary interiors[2,3] and large parts of inertial confinement fusion capsule implosions[4,5] reside. Laboratory experiments to study WDM often span a large portion of the density-temperature parameter space, evolving through the strongly coupled plasma phase, a phase which poses great challenges to current theory.

A strongly coupled plasma[6–8] can be described by the Coulomb coupling parameter, Γ_{ii}, which is taken as the ratio of the average potential energy, <V>, over the average kinetic energy, <K>:

$$\Gamma_{ii} = \frac{< V >}{< K >} = \frac{Z_i^2 e^2}{4\pi\epsilon_0 a} \times \frac{1}{k_B T} > 1, \qquad (1)$$

where Z_i is the mean ionic charge, e is the electron charge, a is the interparticle spacing, k_B the Boltzmann constant, and T the plasma temperature. In the case of a strongly coupled plasma, Γ_{ii} >1, characterized by the Coulomb forces dominating over the thermal excitation of the particles.

Many properties of a strongly coupled plasma are described by the pair correlation function, $g(r)$. This is the probability of finding two ions separated by the distance r. Figure 1 shows $g(r)$ as a function of inter particle distance r for a number of different plasma conditions, ranging from ideal plasma (gas) to an ideal solid (crystal). In an ideal plasma (gas), the ions are distributed around a test ion following Boltzmann's relation. The probability of finding another ion at large distances is unity. In an ideal crystalline solid, the ions are distributed in a three-dimensional lattice. Another ion will be found at a distance r if if is an integer multiple of the d_{hkl} lattice spacing. $g(r)$ shows sharp features at resonances corresponding to the arrangement of the ions in the lattice. The strongly coupled plasma exists somewhere in the middle: neither is it an ideal gas nor a solid. $g(r)$ vanishes at small r due to strong Coulomb repulsion, and approaches 1 at very large distances, where it is screened from interac-

[a)] Corresponding author email: ma8@llnl.gov

tions with the particle at the origin. At radii in-between, there are pronounced peaks and valleys representing correlations, or short-range order, in the plasma.

The accurate characterization of materials in this moderately strong interparticle coupling phase is necessary to broaden our understanding of these transient states and enables the testing of dense plasma models and provide validation for equation of state (EOS) models. To examine such correlations, X-Ray Thomson Scattering (XRTS)[9] can be applied to directly probe the conditions of matter. In XRTS, an intense line x-ray source is sent into the plasma, and the scattering of those x-rays by the electrons of the plasma are observed to give an accurate measurement of electron density, temperature, and ionization state. From momentum and energy conservation, the scattering wave number, $\mathbf{k}$, which is inversely related to the plasma screening length, is given by

$$k = |\mathbf{k}| = \frac{4\pi E_0}{hc} \sin\frac{\theta_s}{2} \tag{2}$$

where E_0 is the incident energy of the probe x-rays, θ_s is the scattering angle, h is Planck's constant and c the speed of light.

The full spectral scattering response is described by the total electronic dynamic structure factor[10,11],

$$S(k,\omega) = |f(k)+q(k)|^2 S_{ii}(k)\delta(\omega) + Z_f S_{ee}(k,\omega) + Z_C \int S_{CE}(k,\omega-\omega')S_S(k,\omega')d\omega' \,. \tag{3}$$

Here, $S_{ii}(k)$ is the static ion structure factor, $S_{ee}(k,\omega)$ corresponds to the dynamic structure factor of the free electrons in the system, $S_{ce}(k,\omega)$ is the structure factor of the core electrons, and $S_s(k,\omega)$ is the self-motion of the ions. The first term of the equation, which accounts for the full response of electrons that dynamically follow the ion motion, includes the contributions of both the bound electrons, represented by the ion form factor $f(k)$ and the screening cloud of free and valence electrons that surround the ion represented by $q(k)$. The second term describes the response of free electrons that do not follow the ionic motion, while the final term of the equation includes inelastic scattering by bound electrons.

These terms will then manifest in a spectrally resolved XRTS spectrum with elastic scattering occurring at the incident x-ray energy, a Compton feature which is downshifted from the incident radiation according to the Compton effect, and a bound-free feature that shows up as a red wing tail. The dynamic structure factor thus contains details of the correlated many-particle system. Within this framework, we can apply energy-resolved x-ray scattering to tease out the details of the system. In particular, in a scattering experiment, we can measure the static structure factor $S(k)$, which is related to the Fourier transform of $g(r)$.

Using XRTS, we can now directly probe the structure of hot dense materials in their strongly coupled state. Such experiments are necessary to test the different models of ion correlations[12,13]. For example, Figure 2 shows four different model predictions of the static ion-ion structure factor (a) and total elastic scattering (b) for Aluminum at 10 eV, 3× compression, and average ionization state of 3. These models primarily vary in their approximation of the inter-particle potential, a large unknown in WDM, and an input quantity in all applied codes[14,15].

The Debye-Hückel (DH) model[8] is a first order plasma approximation. As seen in Fig. 2, the DH model does not predict any correlation peaks in the plasma. In the Screened One Component Plasma (SOCP) model[8], electrons form a polarizable, neutralizing background, and ions are modeled as charged hard spheres, with strong coupling taken into account. Two Hyper-Netted Chain (HNC) calculations using different pseudopotentials are also shown: HNC-Y uses a screened Coulomb Yakawa potential, while HNC-Y+SRR additionally includes a short range repulsive interaction between two atoms at short distances[14,16,17]. In all of these cases, there are subtle differences in the ion-ion structure factor predicted, with oscillations and a primary peak at 4 Å^{-1}. The amplitude of all these peaks depends on the model, and in particular, with SRR, we get a well-pronounced maximum and a large correlation hole at <3 Å^{-1}. Experiments can benchmark these model calculations and thus improve our understanding of warm dense matter conditions.

ADD THIS IN SOMEWHERE? A similar effect also leads to strong modifications in the screening cloud $q(k)$ which may result in negative Fourier components of the electron density[17].

II. MULTI-SHOT MAPPING OF THE CORRELATION PEAK AT OMEGA

The experiment to measure the scattering at varying $\mathbf{k}$ for a single compressed plasma condition was carried out at the OMEGA-60 laser at the Laboratory for Laser Energetics[18]. A schematic of the scattering package target is illustrated in Fig. 3. To launch a strong shock wave into the 125 μm thick aluminum foil targets, nine beams with a total energy of 4.5 kJ were incident onto the foil in a stacked 1 ns square pulse. These beams employed SG4 distributed phase plates to achieve a smooth 800 μm focal spot, and a total drive intensity of 3×10^{14} W/cm^2

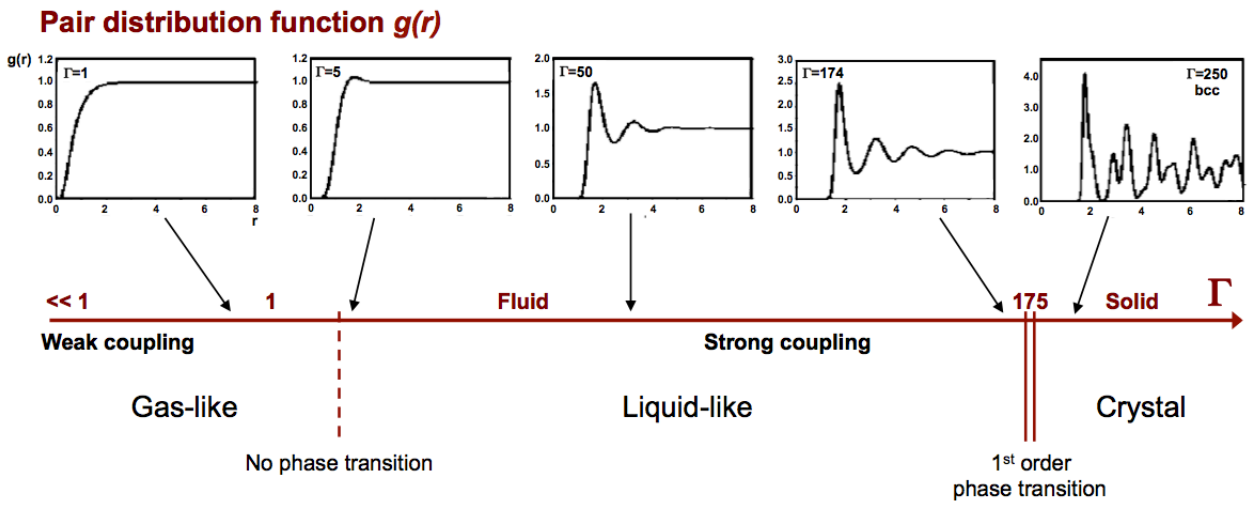

FIG. 1. The pair distribution function $g(r)$ plotted for a number of different plasma conditions, ranging from ideal gas to ideal solid. The strongly coupled plasma exhibits properties common to both gas and solid. *Courtesy of G. Gregori.*

on the sample. 2-D radiation-hydrodynamic calculations using the HYDRA code[19] indicate this laser configuration compressed the aluminum to above three-fold solid density with pressures of 30–40 Mbar. Approximately 3 ns is required for the shock to fully propagate across the 125 μm thick Al foil.

To probe the shocked Al, an x-ray source of molybdenum He-α was generated. These x-rays were created using 15 beams of 1 ns duration, 80 μm focal spot incident on a thin (12 μm) molybdenum foil. For many shots, a single beam of 500 J, defocused to a 200 μm focal spot, 1 ns duration preceded the group of 15 beams by 1 ns. This pre-pulse produced a low-density pre-plasma such that when the main bundle arrived, it would interact with a low density, heated plasma decreasing the amount of cold Kα x-ray radiation produced and boosting the conversion into Mo He-α. An absolutely calibrated Transmission Crystal Spectrometer[20,21] monitored the output of the probe source in first order on each shot. An example of the spectrum is shown in Fig. 4. The strongest line is He-α, Kα, and other 2→1 transitions. From shot-to-shot, the variation in x-ray intensity of the Mo He-α source centered at 17.9 keV was found to not vary by more than 13%. It is estimated that Mo He-α was generated with a laser-to-x-ray energy conversion efficiency of $1-2\times10^{-5}$.

A tantalum aperture of area 0.11 – 0.22 mm^2 between the molybdenum and aluminum foils served to confine the regions being probed by the molybdenum x-rays to the laser irradiated, compressed Al, and restrict the k-vector blurring by limiting the size of the source. Further, for any given shot, by moving the vertical location of the aperture relative to the source of molybdenum probe x-rays, the incident k-vector intersecting the shocked region could be changed to allow for the different scattering k.

This novel target design allowed x-ray scatter in two directions to be simultaneously observed. Large gold foils provided shielding in both the upwards and downwards direction for two curved highly oriented pyrolytic graphite (HOPG)[22] spectrometers with spectral resolution $\lambda/\Delta\lambda$ ∼175, coupled to a microchannel-plate-based gated framing camera with 250 ps temporal resolution. The gold shields limited the scattered emission to a narrow cone, to restrict the scattered k-vectors to those only emerging from the shocked Al region. Also, they prevented x-rays from the backlighter source directly hitting the detector.

Four examples of the raw scattering data recorded at several scattering angles are shown in Fig. 5(a). The scattering signal is the sum of both the elastically scattered photons and inelastically scattered photons from free and weakly bound electrons downshifted in energy. Figure 5(b) shows the line out of two different scattering spectra (69° and 111°) and the difference in the relative ratios of elastic to inelastic features.

Both forward and backward scattering is used to achieve scattering angles ranging from 25° to 135°, corresponding to scattering wave vectors spanning from 2.8 Å^{-1} to 16.5 Å^{-1}, and Compton energies that range from 30 eV to 1.2 keV. As we are in the non-collective regime, the contribution of the free electrons that carry the information on the temperature of the dense plasma is measured in the Compton scattering feature. At the low k-vectors, where the Compton shift is low, the scattering is dominated by contributions from the bound electrons. These bound electrons, with ionization energies larger than $(\hbar k)^2/2m_e$ cannot be excited, and no energy is transferred during the scattering process. The corresponding spectral feature is an un-shifted elastic scattering component at E_0, the Rayleigh peak.

The experimental data shown in Fig. 5 exhibits a systematic reduction in relative scattering intensity as the Compton energy increases for higher angles and the Compton feature shifts further from the elastic peak.

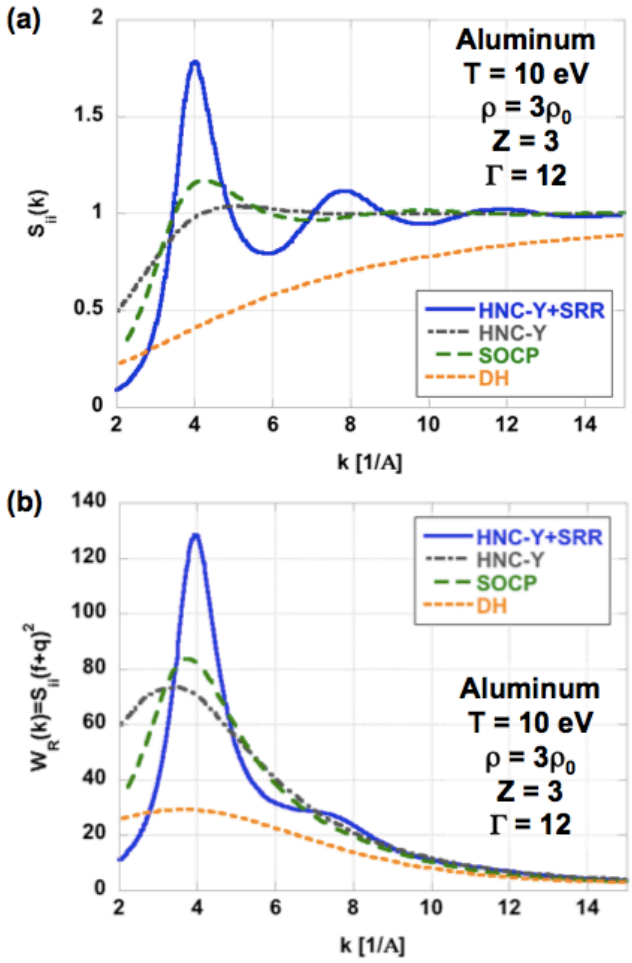

FIG. 2. The static ion-ion structure factor, S_{ii} (a) and the total elastic scattering, $W_R(k)$ (b) as a function of scattering wave number k, as predicted by several models that vary in the form of the interaction potential approximated.

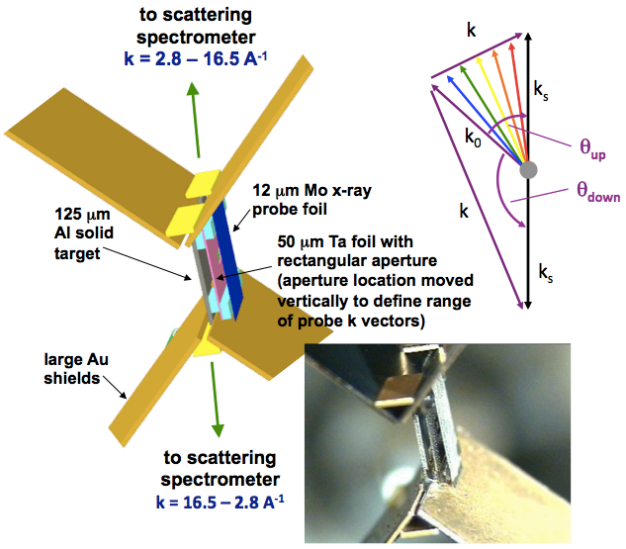

FIG. 3. Schematic and image of the scattering package used at Omega in the multi-shot experiments completed at Omega. This target design allowed for simultaneous forward and backward scattering over a range of k vectors.

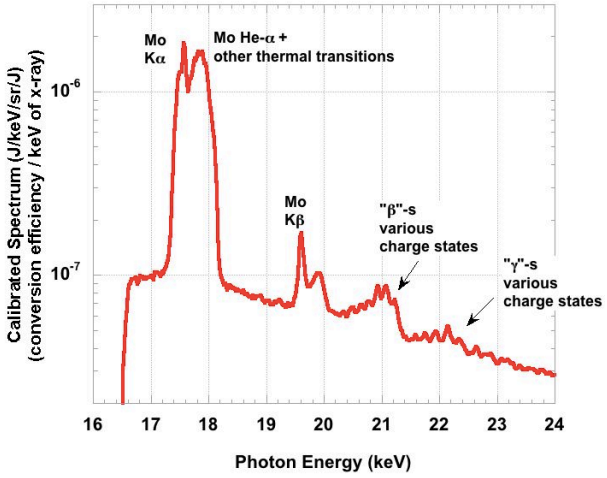

FIG. 4. The molybdenum x-ray spectrum used as a probe. Conversion efficiency into 17-18 keV Mo lines is estimated to be $1-2\times10^{-5}$

The ratio of the elastic to inelastic feature intensity varies with k as expected (dominated by the change in the ion form factor $f(k)$), and at small k, the signal is dominated by the elastically scattered photons.

The 69° spectrally resolved scattering spectra line-out is shown in Fig. 6, with the best fits from synthetic spectra generated from the theoretical form factor of Refs.[8,23] convolved with the spectral distribution of the incident x-ray photons. The individual contributions from elastic, free-free, and bound-free scattering are illustrated. The free electron feature is derived with the random phase approximation and the bound-free and ion peaks are fitted consistent with the analytical screened one component plasma model (SOCP)[8]. The experimental spectra have been background corrected and smoothed over 100 eV. The fit takes into account the detailed spectral features of the Mo source and instrument broadening. Similar fits were found for the full set of experimental scattering spectra taken at the various scattering angles, and good theoretical fits were found at an electron density of 5.4×10^{23} cm^{-3}, $T_i = T_e = 10$ eV, and a mean ion charge, $Z = 3$, in agreement with the HYDRA radiation-hydrodynamic modeling.

The sensitivity of the fits to varying the average ionization, Z, while the mass density is held constant, is shown in the inset of Fig. 6. The spectra show that the red shoulder of the inelastic feature is mainly determined by bound-free scattering. As the ionization state increases, so does the free electron density. Generally, for noncollective scattering, the inelastic feature broadens with the number of free electrons. However, in this case, there are competing mechanisms that increase the intensity of the free-free feature as the bound-free drops:

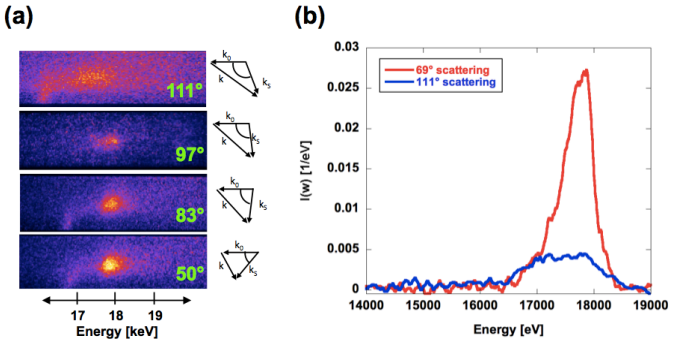

FIG. 5. (a) Experimentally measured scattering data for 50°, 83°, 97°, and 111° scattering angles. (b) Lineouts of the spectrally resolved scattering data 69° (k = 10.3 Å^{-1}) and 111° (k = 15.0 Å^{-1}), in absolute intensity units of I(ω).

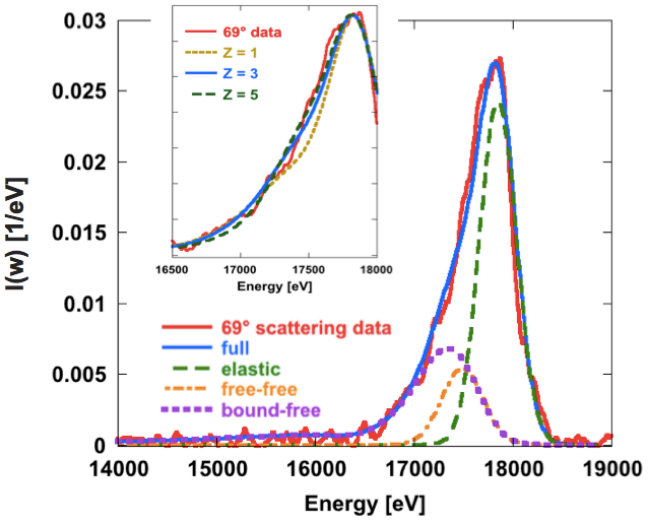

FIG. 6. Comparison of x-ray scattering data at 69° scattering to synthetic spectra best fit at conditions assuming a temperature of 10 eV, electron density of 5.4×10^{23} cm^{-3}, and average ionization state of $Z = 3$. The inset shows the Z sensitivity in the fitting.

(a) the ionization potential is shifting as more and more electrons become mobilized through ionization, and (b) screening by free electrons. This provides a sensitive dial to fitting the full spectra both the free-free and bound-free components must be matched to infer the ionization state.

The absolute intensity of the dynamic structure factor, $S_{ee}(k,\omega)$, is determined from the integral of the spectrally resolved XRTS scattering spectrum for each scattering angle. Corrections are made to the measured scattered power for the polarization of the incident radiation (light from a laser-plasma source is unpolarized, so at a given scattering angle, only a fraction of the incident radiation is contributing to the incident scattering x-ray power), length of the scattering volume (and subsequent attenuation of the probe x-rays through the compressed

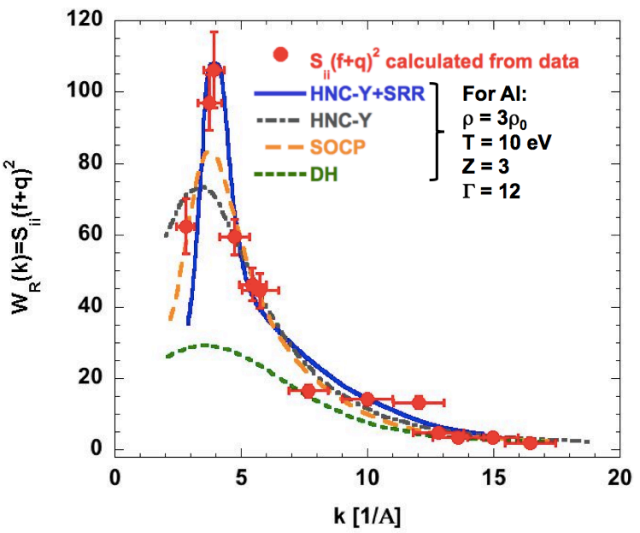

FIG. 7. The strong increase of the elastic scattering signal to a maximum of $W_R(k) = (f+q)^2 S_{ii}) = 106$ at a $k = 4$ Å^{-1} is in agreement with calculations from with simulations that incorporate short-range repulsion.

material), and solid angle of the scattering volume (due to slight changes in target geometry to achieve the various scattering angles).

The amplitude of the elastic scattering is determined by subtracting the free-free and bound-free components. The free-free contribution is directly calculated from a $< Z > /(1+\alpha^2)$ scaling, and the contribution from transitions of core electrons into the continuum (bound-free) is analytically derived as described in Gregori, *et al.*[11].

The measured strength of the elastic scattering ($W_R(k) = (f+q)^2 S_{ii}$) as a function of scattering vector k for the shock-compressed aluminum with a mass density of $\rho = 8.1$ g/cm^3 and temperature of 10 eV exhibits a sharp maximum at $k = 4$ Å^{-1} , as shown in Fig. 7. Analytical calculations in the form of the Debye-Hückel plasma approximation fail to capture the clear trend seen in the experimental data, implying that the DH model cannot describe the strong ion-ion correlations. The SOCP model predicts a pronounced peak at the right location, with an approximate width of the correct span, but underestimates the absolute amplitude of the correlation peak.

Only an explicit calculation for strong coupling, the HNC-Y+SRR, gives overall good agreement with the experimentally measured data. Here, the screened Coulomb interactions are modified by an additional short range repulsive factor in the interaction, as fitted to ab initio simulations[14]. This indicates that both short range repulsion and screening effects are very important in this regime.

The measurement of the k dependence of the elastic scattering feature can further serve as a valuable diagnostic for characterizing compressed states of matter. As the peak position is inversely proportional to the ion-ion

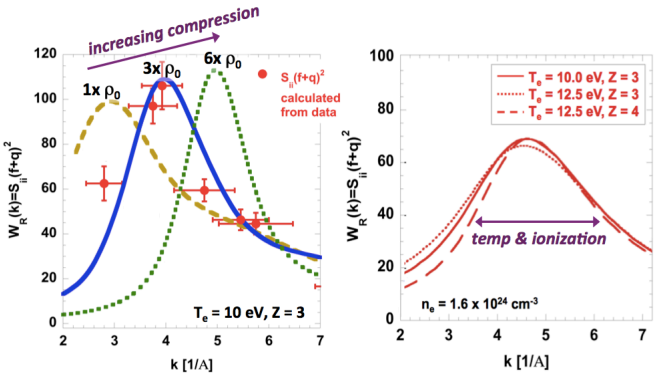

FIG. 8. The elastic scattering amplitude peak shifts and changes with material compression, while the width changes with temperature and ionization state.

distance, mapping out the location of this peak serves as a density diagnostic of the compressed plasma. With increasing degree of compression, the elastic scattering amplitude shifts to larger wave number and higher peak intensity. With varying temperature and ionization, the position of the peak does not deviate significantly, but the width changes. See Fig. 8 for calculations completed with HNC-Y+SRR.

III. SINGLE-SHOT MAPPING OF THE CORRELATION PEAK AT LCLS

The recent commissioning of the Matter in Extreme Conditions (MEC) instrument[24] at the Linac Coherent Light Source (LCLS)[25], presents a new capability to conduct experiments to investigate the properties of WDM. In particular, the high peak brightness of the LCLS X-ray Free Electron laser (XFEL) introduces the ability to directly probe compressed materials at a chosen tuned wavelength, without having to generate such a high-energy x-ray source with a laser. While this is a smaller scale experiment, the experimental setup is considerably simplified as the LCLS beam is highly collimated (10 μm spot size), of a pulse duration of 20–100 fs, and bandwidth of $\Delta E/E = 0.2$–0.5% at a photon energy of $E_0 = 8$ keV.

One or two 527 nm long-pulse lasers of 8×10^{13} W/cm^2 drive single- or counter-propagating shocks with a 3 ns square pulse into an Al sample of 50 μm thickness. The time delay of the incident LCLS beam is varied to probe various shock conditions in the Al as the shocks propagate, coalesce, then decompress.

On every shot, a suite of diagnostics measures the scattering from the Al sample: collective (forward) and non-collective (backward) scattering spectrometers with curved highly-annealed pyrolytic graphite (HAPG) in a Von Hamos geometry[26] record the spectra. Several large area detectors (the Cornell Stanford Pixel Array Detector, CSPAD)[27] provide frequency-integrated, angularly resolved diffraction patterns. For cold, uncompressed material, diffraction occurs off the ambient ion-lattice, giving Debye-Scherrer cone projections[28]. As the material is heated and compressed, the sharp Bragg peaks disappear and scattering follows the correlation peak. The evolution of the compressed material can then be tracked, as the correlation peak moves to larger scattering angles as the density increases. With each shot, full wave-number resolution of the amplitude of the elastic scattering is recorded. Future publications will describe this in detail.

IV. CONCLUSIONS

Aluminum, which has been extensively studied due to its wide industry use and abundance in the earth's crust, serves as an excellent material for which to validate theoretical models that predict strong correlations very different from the classical flat plasma behavior, and which is typically expected in the warm dense matter regime[12,14]. We have used x-ray Thomson scattering at 17.9 keV to probe a compressed aluminum. The angularly resolved elastic amplitudes were compared with analytical calculations and predictions based on calculations with an HNC model incorporating Yakawa potential screening and short range repulsion, and it was found that screening effects must be accounted for in order to fit the shape of the data and the absolute intensity. Using XRTS we fully resolve the ion-ion correlation as a function of scattering k, providing a precise measurement of the structure of warm dense matter. The method of mapping out the elastic scattering amplitude as a function of k gives a direct measurement of compression in laser-shocked aluminum. Further, we have demonstrated single shot measurements of the angularly resolved scattering affording a new dynamic density diagnostic.

V. FUTURE WORK

This methodology has now been applied to a number of different types of materials to measure their dynamic structure factors at different conditions. One such application that is particularly promising and well-suited to the use of XRTS is the search for the electride state of matter, a new material phase predicted by Density Functional Theory (DFT) under high-pressure conditions[29,30]. In the electride phase, the valence electrons, instead of becoming delocalized and Fermi degenerate as may be expected, are believed to actually bunch up in interstitial pockets within the still persisting ion lattice. Such systems would represent a completely new material phase, with new optical, electrical, and magnetic properties.

Laser-induced shock-wave experiments provide a valuable platform to achieve these temperature and density conditions. By using XRTS, direct experimental verification of the existence of the electride state can be provided

by measuring dynamic electronic and ionic structure factors. A peak will emerge in the overall scattering intensity at the wavenumber corresponding to the spacing associated with the electride lattice. Work on this topic is the subject of ongoing studies.

VI. ACKNOWLEDGEMENTS

This work was performed under the auspices of the U.S. Department of Energy by Lawrence Livermore National Laboratory under Contract DE-AC52-07NA27344.

[1] *Frontiers in High Energy Density Physics: The X-Games of Contemporary Science* (The National Academies Press, 2003).
[2] L. R. Benedetti, Science **286**, 100 (1999).
[3] M. Ross, Nature **292**, 435 (1981).
[4] M. J. Edwards, J. D. Lindl, B. K. Spears, S. V. Weber, L. J. Atherton, D. L. Bleuel, D. K. Bradley, D. A. Callahan, C. J. Cerjan, D. Clark, et al., Physics Of Plasmas **18**, 051003 (2011).
[5] S. H. Glenzer, D. A. Callahan, A. J. Mackinnon, J. L. Kline, G. Grim, E. T. Alger, R. L. Berger, L. A. Bernstein, R. Betti, D. L. Bleuel, et al., Physics Of Plasmas **19**, 056318 (2012).
[6] D. Kremp, M. Schlanges, and W.-D. Kraeft, *Quantum Statistics of Nonideal Plasmas* (Springer, 2005).
[7] M. S. Murillo, Physics Of Plasmas **11**, 2964 (2004).
[8] G. Gregori, A. Ravasio, A. Höll, S. Glenzer, and S. Rose, High Energy Density Physics **3**, 99 (2007).
[9] S. Glenzer, G. Gregori, R. Lee, F. Rogers, S. Pollaine, and O. Landen, Physical Review Letters **90**, 175002 (2003).
[10] J. Chihara, Journal of Physics: Condensed Matter **12**, 231 (2000).
[11] G. Gregori, S. Glenzer, W. Rozmus, R. Lee, and O. Landen, Physical Review E **67**, 026412 (2003).
[12] K. Wünsch, P. Hilse, M. Schlanges, and D. O. Gericke, Physical Review E **77**, 056404 (2008).
[13] T. Ma, T. Doppner, R. W. Falcone, L. Fletcher, C. Fortmann, D. O. Gericke, O. L. Landen, H. J. Lee, A. Pak, J. Vorberger, et al., Physical Review Letters **110**, 065001 (2013).
[14] K. Wünsch, J. Vorberger, and D. O. Gericke, Physical Review E **79**, 010201 (2009).
[15] J. Vorberger and D. O. Gericke, High Energy Density Physics **9**, 178 (2013).
[16] K. Wünsch, J. Vorberger, G. Gregori, and D. O. Gericke, Journal of Physics A: Mathematical and Theoretical **42**, 214053 (2009).
[17] D. O. Gericke, J. Vorberger, K. Wünsch, and G. Gregori, Physical Review E **81**, 065401 (2010).
[18] T. R. Boehly, R. S. Craxton, T. H. Hinterman, J. H. Kelly, T. J. Kessler, S. A. Kumpan, S. A. Letzring, R. L. Mccrory, S. F. B. Morse, W. Seka, et al., Review of Scientific Instruments **66**, 508 (1995).
[19] M. M. Marinak, G. D. Kerbel, N. A. Gentile, O. Jones, D. Munro, S. Pollaine, T. R. Dittrich, and S. W. Haan, Physics Of Plasmas **8**, 2275 (2001).
[20] J. Seely, G. Holland, L. Hudson, C. Szabo, A. Henins, H. S. Park, P. K. Patel, R. Tommasini, and J. Martinlaming, High Energy Density Physics **3**, 263 (2007).
[21] C. Szabo, U. Feldman, S. Seltzer, L. Hudson, M. O'Brien, H. Park, and J. Seely, Optics Letters **36**, 1335 (2011).
[22] A. Pak, G. Gregori, J. Knight, K. Campbell, D. F. Price, B. Hammel, O. L. Landen, and S. H. Glenzer, Review of Scientific Instruments **75**, 3747 (2004).
[23] S. Ichimaru, Reviews of Modern Physics **54**, 1017 (1982).
[24] L. Fletcher, Science (in preparation, 2014).
[25] J. Amann, W. Berg, V. Blank, F. J. Decker, Y. Ding, P. Emma, Y. Feng, J. Frisch, D. Fritz, J. Hastings, et al., pp. 1–6 (2012).
[26] U. Zastrau, A. Woldegeorgis, E. Forster, R. Loetzsch, H. Marschner, and I. Uschmann, Journal of Instrumentation **8**, P10006 (2013).
[27] P. Hart, S. Boutet, G. Carini, M. Dubrovin, B. Duda, D. Fritz, G. Haller, R. Herbst, S. Herrmann, C. Kenney, et al., in *SPIE Optical Engineering + Applications*, edited by S. P. Moeller, M. Yabashi, and S. P. Hau-Riege (SPIE, 2012), pp. 85040C–85040C–11.
[28] D. Milathianaki, S. Boutet, G. J. Williams, A. Higginbotham, D. Ratner, A. E. Gleason, M. Messerschmidt, M. M. Seibert, D. C. Swift, P. Hering, et al., Science **342**, 220 (2013).
[29] C. J. Pickard and R. J. Needs, Nature Materials **9**, 624 (2010).
[30] C. Fortmann, C. Niemann, and S. Glenzer, Physical Review B **86**, 174116 (2012).